



# Co<sub>3</sub>O<sub>4</sub> nanoparticles-loaded BiOCl nanoplates with the dominant {001} facets: efficient photodegradation of organic dyes under visible light

Congwei Tan<sup>a</sup>, Gangqiang Zhu<sup>a,\*</sup>, Mirabbos Hojamberdiev<sup>b</sup>, Kiyoshi Okada<sup>b</sup>, Jia Liang<sup>a</sup>, Xiancong Luo<sup>a</sup>, Peng Liu<sup>a</sup>, Yun Liu<sup>c</sup>

<sup>a</sup> School of Physics and Information Technology, Shaanxi Normal University, Xi'an 710062, PR China

<sup>b</sup> Materials and Structures Laboratory, Tokyo Institute of Technology, 4259 Nagatsuta, Midori, Yokohama, Kanagawa 226-8503, Japan

<sup>c</sup> School of Materials Science and Engineering, Shaanxi University of Science and Technology, Xi'an 710068, PR China

## ARTICLE INFO

### Article history:

Received 25 September 2013

Received in revised form 17 January 2014

Accepted 26 January 2014

Available online 4 February 2014

### Keywords:

Cobalt oxide

Bismuth oxychloride

Heterojunction

Photocatalyst

Visible light

## ABSTRACT

In this work, a facile method was developed to improve the photocatalytic efficiency of bismuth oxychloride (BiOCl) with the dominant {001} facets and cobalt oxide (Co<sub>3</sub>O<sub>4</sub>) through creating a heterojunction between them. The heterostructured Co<sub>3</sub>O<sub>4</sub>/BiOCl photocatalyst with different amounts of Co<sub>3</sub>O<sub>4</sub> (0, 0.4, 0.8, 1.2, and 1.6 wt%) was successfully synthesized by a simple chemical co-precipitation method. The as-synthesized samples were characterized by X-ray diffraction (XRD), scanning electron microscopy (SEM), transmission electron microscopy (TEM), X-ray photoelectron spectroscopy (XPS), UV-vis spectroscopy (UV-vis), Brunauer–Emmett–Teller (BET), and photoluminescence spectroscopy (PL). Due to the formation of the heterojunction, which grows along the [001] crystallographic direction of BiOCl, the effective separation of electron-hole pairs results in the enhanced photocatalytic activity of the Co<sub>3</sub>O<sub>4</sub>/BiOCl system. The 0.8 wt% Co<sub>3</sub>O<sub>4</sub>/BiOCl exhibits the highest photocatalytic activity as compared with other samples (0, 0.4, 1.2, and 1.6 wt% Co<sub>3</sub>O<sub>4</sub>/BiOCl) because of the enhanced flow of charge carriers through the heterojunction, and light absorbance. The photodegradation mechanisms of Rhodamine B (RhB) and methyl orange (MO) over the heterostructured Co<sub>3</sub>O<sub>4</sub>/BiOCl photocatalyst under visible light was also studied, and the enhanced photocatalytic activity could be attributed to the improved separation of photo-induced electron-hole pairs by creating the heterojunction along the [001] crystallographic direction. According to the results obtained from the recyclability experiments, the heterostructured Co<sub>3</sub>O<sub>4</sub>/BiOCl photocatalyst could be easily recycled without decreasing photocatalytic activity due to its high photostability.

© 2014 Elsevier B.V. All rights reserved.

## 1. Introduction

Since Fujishima and Honda first reported photocatalysis on a TiO<sub>2</sub> electrode, semiconductor-based photocatalysis has been attracting much attention for environmental remediation and renewable energy [1,2]. As visible light occupies the major portion of solar light, improving the efficiency of visible light-responsive photocatalysts has become one of the most focused topics in contemporary photocatalysis field. As known, photocatalysis occurs when the photocatalyst absorbs a photon of energy equivalent to or higher than the band-gap energy ( $E_g$ ) of the semiconductor, and photo-induced electron-hole pairs are then created [3,4]. An electron in the valence band (VB) is transited into the conduction band

(CB), leaving a hole in the VB, simultaneously. The photo-generated electron-hole pairs then react with the adsorbed molecules (e.g., water, oxygen, hydroxyl, etc.) on the surface/interface of the photocatalyst, ultimately producing the highly oxidizing radical species (e.g.,  $\bullet\text{O}_2^-$ ,  $\bullet\text{OH}$ ), which can further oxidize organic molecules into carbon dioxide, water and inorganic products. However, there are still several pivotal questions concerning practical applications: (i) to reduce the cost of production for the purpose of commercialization, (ii) to develop photocatalytic ability for the degradation of various organic dyes, (iii) to decrease a high rate of electron-hole pair recombination and low interfacial charge transfer.

To overcome such formidable obstacles, we often consider employing two effective and simple strategies: (i) cation and anion doping (e.g., Fe, Pt, Ag) and (ii) creating a heterostructure by combining two semiconductors (e.g., LaVO<sub>4</sub>/TiO<sub>2</sub> [5], TiO<sub>2</sub>/V-TiO<sub>2</sub> [6], NiO/ZnO [7], etc.). Although cation and anion doping route shows enhanced photocatalytic activity under visible light, the rapid recombination of electron-hole pairs impairs photocatalytic

\* Corresponding author. Tel.: +86 29 81530750; fax: +86 29 81530750.

E-mail address: [zgq2006@snnu.edu.cn](mailto:zgq2006@snnu.edu.cn) (G. Zhu).

activity [5,8]. Because of photo-corrosion and an increase in charge carrier recombination rate, traditional visible light-active photocatalysts with narrow band gaps have low photocatalytic activity [8]. Thus, a great vision has come toward the creation of a heterojunction by combining two different semiconductors [4,9].

Compared with the impurity doping method, the creation of a heterojunction with two different semiconductors having two different band gap structures is more flexible for broadening visible light absorption and less sensitive to the component homogeneity [10,11]. Therefore, upon the formative heterojunction, the photo-induced electron-hole pairs can quickly migrate to the surface/interface, lessen the possibility of recombination, improving the photocatalytic performance [12,13]. Nevertheless, the application of a heterojunction for enhancing the photodegradation of organic pollutants still faces some obstacles, namely: (i) the production process is complex and needs to be simplified and (ii) dye photodegradation by indirect semiconductor photosensitization process is low [4–7]. Therefore, the creation of a heterojunction growing along the determined crystallographic direction will be another option to solve those issues. In this context, we therefore emphasize mainly on the enhancement of photocatalytic activity by creating the heterojunction between BiOCl nanoplates with the dominant {001} facets and  $\text{Co}_3\text{O}_4$  nanoparticles.

With a wide band gap ( $E_g = 3.4 \text{ eV}$ ), bismuth oxychloride (BiOCl) has recently evoked much interest due to its good photocatalytic activity under UV light, unique layered structure, and high photo-corrosion stability [14–17]. Generally, the intrinsic property of BiOCl limits its efficient utilization of visible light in the photodegradation of organic dye molecules. Nonetheless, the BiOCl has a layered structure composing of  $[\text{Bi}_2\text{O}_2]^{2+}$  layers between two sheets of Cl ions [18,19], the self-induced internal electric fields or perpendicular to the {001} facets of the BiOCl caused by  $[\text{Bi}_2\text{O}_2]^{2+}$  cation layer [4,18,20]. This kind of architecture facilitates an easy transfer of electrons. Hence, the charge separation and transfer assisted by the internal electric field are more favorable along the [001] crystallographic direction. Moreover, the negative {001} facets terminated with oxygen can naturally enhance the adsorption of cationic dyes, such as RhB [21] and improve significantly the efficiency of photosensitized degradation process. Although it has shown the negative adsorption of ionic dye, such as methyl orange (MO) [18], the indirect dye-photosensitized degradation process can also describe the photo-reactivity of BiOCl [20], and the internal electric fields can inhibit the recombination of photo-induced electron-hole pairs in order to enhance the photodegradation of MO. Till now, BiOCl has been combined with other narrow band-gap semiconductors to improve its photocatalytic performance. Particularly, nano-flaked BiOCl heterostructured with  $\text{Bi}_2\text{O}_3$  [12,15,22], BiOI [23],  $\text{WO}_3$  [24], and  $\text{NaBiO}_3$  [25] demonstrated efficient separation of electron-hole pairs and enhanced photocatalytic activity for the photodegradation of 1,4-terephthalic acid (TPA), nitric oxide (NO), RhB, and MO, respectively.

$\text{Co}_3\text{O}_4$  is a *p*-type semiconductor with interesting electronic properties [26] and has a narrow band gap ( $\sim 2.07 \text{ eV}$ ). Due to its excellent properties,  $\text{Co}_3\text{O}_4$  can be applied as high-temperature solar selective absorber and efficient catalyst [27,28]. Zhang et al. [29] reported that the  $\text{Co}_3\text{O}_4$ -coupled  $\text{Ag}_3\text{VO}_4$  showed the improved photocatalytic activity for the photodegradation of RhB under visible light. The  $\text{Co}_3\text{O}_4/\text{BiVO}_4$  exhibited the enhanced photocatalytic performance for the photodegradation of acid orange II under visible light [30]. Like BiOCl,  $\text{Co}_3\text{O}_4$  has also been combined with other semiconductors to create a heterojunction ( $\text{Co}_3\text{O}_4/\text{CeO}_2$  [31],  $\text{Co}_3\text{O}_4/\text{Bi}_2\text{WO}_6$  [32] and so on), resulting in a high photocatalytic activity.

The band gap of  $\text{Co}_3\text{O}_4$  ( $E_g = 2.07 \text{ eV}$ ) is smaller than that of BiOCl ( $E_g = 3.4 \text{ eV}$ ), and the conduction band (CB) of  $\text{Co}_3\text{O}_4$  ( $E_{\text{CB}} = -0.37 \text{ eV}$

versus NHE) [28] is higher than that of BiOCl ( $E_{\text{CB}} = 0.14 \text{ eV}$  versus NHE) [17]. By considering the band gap positions of BiOCl and  $\text{Co}_3\text{O}_4$ , on one hand, the electrons photo-generated from the valence band (VB) of the  $\text{Co}_3\text{O}_4$  can be transferred to BiOCl, and the electrons get accumulated and form internal micro-electric fields between two semiconductors, promoting the migration of photo-generated charge carriers, initiating a photocatalytic reaction. On the other hand, a cooperative effect of surface properties and heterojunction may also enhance the photocatalytic activity of the  $\text{Co}_3\text{O}_4/\text{BiOCl}$  for the photodegradation of organic dyes under visible light. Therefore, not only do the {001} facets represent the ability to transform the electrons but also the internal electric fields extend the interface electric field of a heterojunction which might be accounted for the  $\text{Co}_3\text{O}_4/\text{BiOCl}$  *p-n* heterojunction engendered along the [001] direction of the {001} facet of BiOCl.

In this work, a chemical co-precipitation method was applied to synthesize the  $\text{Co}_3\text{O}_4/\text{BiOCl}$  heterostructured photocatalyst composed of  $\text{Co}_3\text{O}_4$  nanoparticles loaded on the BiOCl nanoplates with the dominant {001} facets. Under visible light irradiation, the  $\text{Co}_3\text{O}_4/\text{BiOCl}$  heterostructured photocatalyst exhibited efficient photocatalytic activity for the photodegradation of cationic (Rhodamine B) and ionic (methyl orange) organic dyes. The photodegradation mechanisms are also proposed.

## 2. Experimental

### 2.1. Synthesis of $\text{Co}_3\text{O}_4/\text{BiOCl}$ heterostructured photocatalyst

All the chemical reagents were of analytical grade and used without further purification. The  $\text{Co}_3\text{O}_4/\text{BiOCl}$  heterostructured photocatalyst was prepared by a simple chemical co-precipitation method at room temperature. In a typical procedure,  $\text{CoCl}_2$  was dissolved in 10 mL of 1 M HCl containing a stoichiometric amount of  $\text{BiCl}_3$ . The pH of the solution was adjusted to 9–10 with the drop-wise addition of aqueous ammonia under vigorous stirring, and the gel-like mixture formed was aged for 2 h before filtration. The resulting precipitate was then filtered and washed with distilled water and ethanol several times, dried at  $80^\circ\text{C}$  for 8 h, and calcined at  $400^\circ\text{C}$  for 1 h. To study the effect of  $\text{Co}_3\text{O}_4$  content on the photocatalytic performance of  $\text{Co}_3\text{O}_4/\text{BiOCl}$  heterostructured photocatalyst, the  $\text{Co}_3\text{O}_4$  amount was varied from 0 to 1.6 wt%.

### 2.2. Characterization

The crystalline phases were identified by X-ray powder diffraction using a D/Max2550 X-ray diffractometer (Rigaku, Japan) with Cu  $K\alpha$  radiation ( $\lambda = 1.5406 \text{ \AA}$ ). The samples were scanned at a scanning rate of  $5^\circ/\text{min}$  in the  $2\theta$  range of  $10\text{--}80^\circ$  at 40 kV and 40 mA. The transmission electron microscopic (TEM) and high-resolution transmission electron microscopic (HRTEM) images of the samples were taken with a JEM-2100 electron microscope (JEOL, Japan) with an acceleration voltage of 200 kV. X-ray photoelectron spectroscopy (XPS) analysis was performed on an ESCALAB MKII X-ray photoelectron spectrometer (VG Scientific, UK) using Mg  $K\alpha$  radiation. The UV-vis diffuse reflectance spectra of the samples were measured using a Lambda 950 UV-VIS-NIR spectrophotometer (Perkin-Elmer, USA) in the wavelength range of 200–800 nm. The specific surface areas ( $S_{\text{BET}}$ ) were obtained from  $\text{N}_2$  adsorption-desorption isotherms at 77 K (ASAP 2010, Micromeritics, USA) on the samples preheated at  $120^\circ\text{C}$  for 12 h in vacuum. The  $S_{\text{BET}}$  values were calculated using the Brunauer, Emmett and Teller (BET) method. The photoluminescence (PL) spectral measurements were conducted using an LS-55 luminescence spectrometer (Perkin-Elmer, USA) with a xenon lamp with the excitation wavelength of 325 nm.

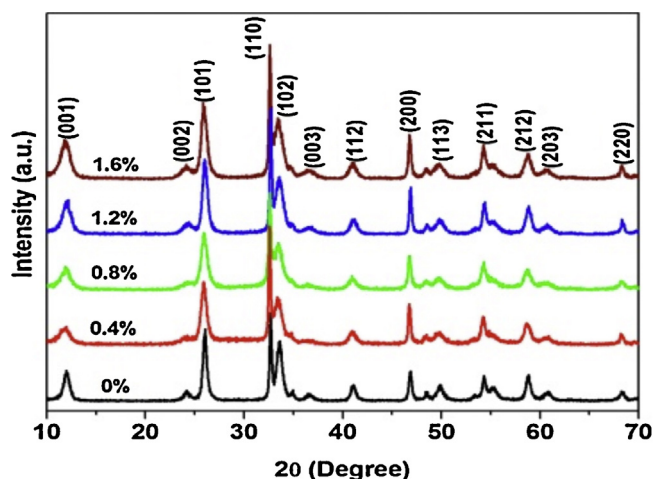


Fig. 1. XRD patterns of the  $\text{Co}_3\text{O}_4/\text{BiOCl}$  samples with different amounts of  $\text{Co}_3\text{O}_4$  ranging from 0 to 1.6 wt%.

### 2.3. Photodegradation experiments

To investigate the photocatalytic performance, cationic (Rhodamine B) and ionic (methyl orange) dyes were chosen as model organic pollutants. The photodegradation of RhB and MO by the prepared samples was performed in a 60 mL glass-tube reactor under visible light using a 400 W tungsten halogen lamp with a 420 nm cutoff filter. The photodegradation reaction temperature was maintained at 25 °C by water flowing through the cooling jacket of the reactor. The initial concentrations of RhB and MO in aqueous solution were 20 mg/L and the photocatalyst sample was 1.0 g/L. First, the photocatalyst sample was dispersed in a glass vial containing 50 mL of RhB/MO aqueous solution, and the suspension was stirred in the dark for 2 h to ensure adsorption–desorption equilibrium prior to visible light irradiation. During the photodegradation reaction, 2 mL of the suspension was taken out at a given time interval for subsequent RhB/MO concentration analysis. The RhB/MO concentration was analyzed by U-3010 UV-vis spectrophotometer (Hitachi, Japan).

## 3. Results and discussion

### 3.1. Structural, morphological and chemical characterization of the $\text{Co}_3\text{O}_4/\text{BiOCl}$ heterostructured photocatalyst

Fig. 1 shows the XRD patterns of the  $\text{Co}_3\text{O}_4/\text{BiOCl}$  heterostructured photocatalyst samples with different amounts of  $\text{Co}_3\text{O}_4$  ranging from 0 to 1.6 wt%. As can be seen in Fig. 1, the XRD patterns of the samples with a low amount of  $\text{Co}_3\text{O}_4$  show only BiOCl crystal phase, and no diffraction peaks assignable to the  $\text{Co}_3\text{O}_4$  phase can be noted. Nevertheless, we still believe that the  $\text{Co}_3\text{O}_4$  nanoparticles were formed and dispersed on the surface of the BiOCl nanoplates. The crystallite sizes estimated from the peak broadening of the samples are nearly the same, confirming that the crystallite sizes of the samples were not influenced by the increased amount of  $\text{Co}_3\text{O}_4$  nanoparticles. Most notably, in the XRD patterns of the  $\text{Co}_3\text{O}_4/\text{BiOCl}$  samples, the (001) diffraction peak of the BiOCl crystal phase broadens with increasing the amount of  $\text{Co}_3\text{O}_4$ , indicating a small size along the [001] crystallographic direction [33–35]. All the diffraction peaks identified in the XRD patterns can be assigned to the tetragonal structure of BiOCl (JCPDS card no. 06-0249) [18]. The intensity ratio of the (110)/(001) diffraction peaks, shown in the XRD patterns, is

attributed to the formation of ultrathin nanoplates oriented along the [001] crystallographic direction, implying a relatively large lateral size oriented along the [001] crystallographic direction [33,34].

To further confirm the existence of  $\text{Co}_3\text{O}_4$  nanoparticles on the surfaces of the BiOCl nanoplates and to analyze the chemical composition and chemical state of the elements, X-ray photoelectron spectroscopy (XPS) analysis was performed. Fig. 2 shows the XPS spectra of the elements present in the  $\text{Co}_3\text{O}_4/\text{BiOCl}$  heterostructured photocatalyst. As can be seen in Fig. 2a, a wide survey scan of the sample clearly indicates the co-presence of only Bi, O, Cl, and Co without other prominent impurities, excluding adventitious carbon-based contaminant. Fig. 2b indicates two bands with binding energies of 159.4 and 164.7 eV that can be assigned to Bi 4f<sub>7/2</sub> and Bi 4f<sub>5/2</sub>, respectively. The asymmetric XPS spectrum of O 1s, shown in Fig. 2c, indicates that the different oxygen species are present in the surface region of the sample. The XPS peak assignable to the lattice oxygen of crystalline BiOCl and  $\text{Co}_3\text{O}_4$  can be noted at 530.8 eV; however, there is another peak which might be ascribed to the surface oxygen of the sample. The Cl 2p orbital shows a peak at 201.0 eV (Fig. 2d). As shown in Fig. 2e, the binding energies for Co 2p<sub>3/2</sub> and Co 2p<sub>1/2</sub> main peaks are found to be at 781.3 and 796.6 eV, respectively. The binding energies obtained in this study for Co 2p<sub>3/2</sub> and Co 2p<sub>1/2</sub> are close to the previously reported binding energies at 780.8 and 796.8 eV [17,30,31]. According to the XPS results, it can be deduced that the  $\text{Co}_3\text{O}_4$  nanoparticles are present in the  $\text{Co}_3\text{O}_4/\text{BiOCl}$  samples. The XRD and XPS results confirm the coexistence of the BiOCl and  $\text{Co}_3\text{O}_4$  phases in the heterostructured photocatalyst.

The microstructural characteristics of the  $\text{Co}_3\text{O}_4/\text{BiOCl}$  heterostructured photocatalyst samples with different amounts of  $\text{Co}_3\text{O}_4$  were examined by a transmission electron microscope (TEM). Fig. 3 shows the TEM micrographs of the  $\text{Co}_3\text{O}_4/\text{BiOCl}$  samples with 0 wt% (a), 0.4 wt% (b), 0.8 wt% (c), 1.2 wt% (e), and 1.6 wt% (f)  $\text{Co}_3\text{O}_4$  nanoparticles and the HRTEM image of the 0.8 wt%  $\text{Co}_3\text{O}_4/\text{BiOCl}$  sample (d). The HRTEM image of a single BiOCl crystal in Fig. 3(a1), viewed from the [001] axis, clearly shows two lattice fringes with a mutual lattice spacing of 0.27 nm, corresponding to the {110} facets and {1 $\bar{1}$ 0} facets. As shown in Fig. 3(a) and (a2), each BiOCl nanoplate has a thickness of ca. 6 nm and a lateral size of ca. 400 nm, implying that the percentage of the {001} facets is estimated to be 97%. The intersection angle between the {110} and {1 $\bar{1}$ 0} facets is 90°, depicting that the BiOCl single crystal exhibits a high percentage of {001} facets exposure, which conform to the XRD data.

In Fig. 3 (b, c, e, and f), the illustrative TEM images of the  $\text{Co}_3\text{O}_4/\text{BiOCl}$  samples with different amounts of  $\text{Co}_3\text{O}_4$  nanoparticles depict that the  $\text{Co}_3\text{O}_4$  nanoparticles are uniformly distributed and attached onto the surface of BiOCl nanoplates. The magnified TEM and HRTEM images of the 0.8 wt%  $\text{Co}_3\text{O}_4/\text{BiOCl}$  sample, shown in Fig. 3d, provide the detailed information about the structure of the heterostructured samples. Different lattice fringes, which are considered for the identification of crystallographic spacing of  $\text{Co}_3\text{O}_4$  and BiOCl viewed from the [001] axis, can be found in the HRTEM image of the sample shown in the inset of Fig. 3d. The lattice fringes with the spacing of  $d=0.27$  nm correspond to the (110) and (1 $\bar{1}$ 0) crystallographic planes of BiOCl, whereas the lattice fringes with the spacing of  $d=0.28$  nm match with the (220) crystallographic plane of  $\text{Co}_3\text{O}_4$ . The TEM results evidence that the  $\text{Co}_3\text{O}_4/\text{BiOCl}$  heterojunction grows along the [001] direction on the flat surface of the BiOCl nanoplates belong to the [001] facets. Moreover, a distinguished interface and continuity of the lattice fringes between the  $\text{Co}_3\text{O}_4$  and BiOCl can be observed in Fig. 3d, suggesting that the  $p$ – $n$  heterojunction was indeed formed between

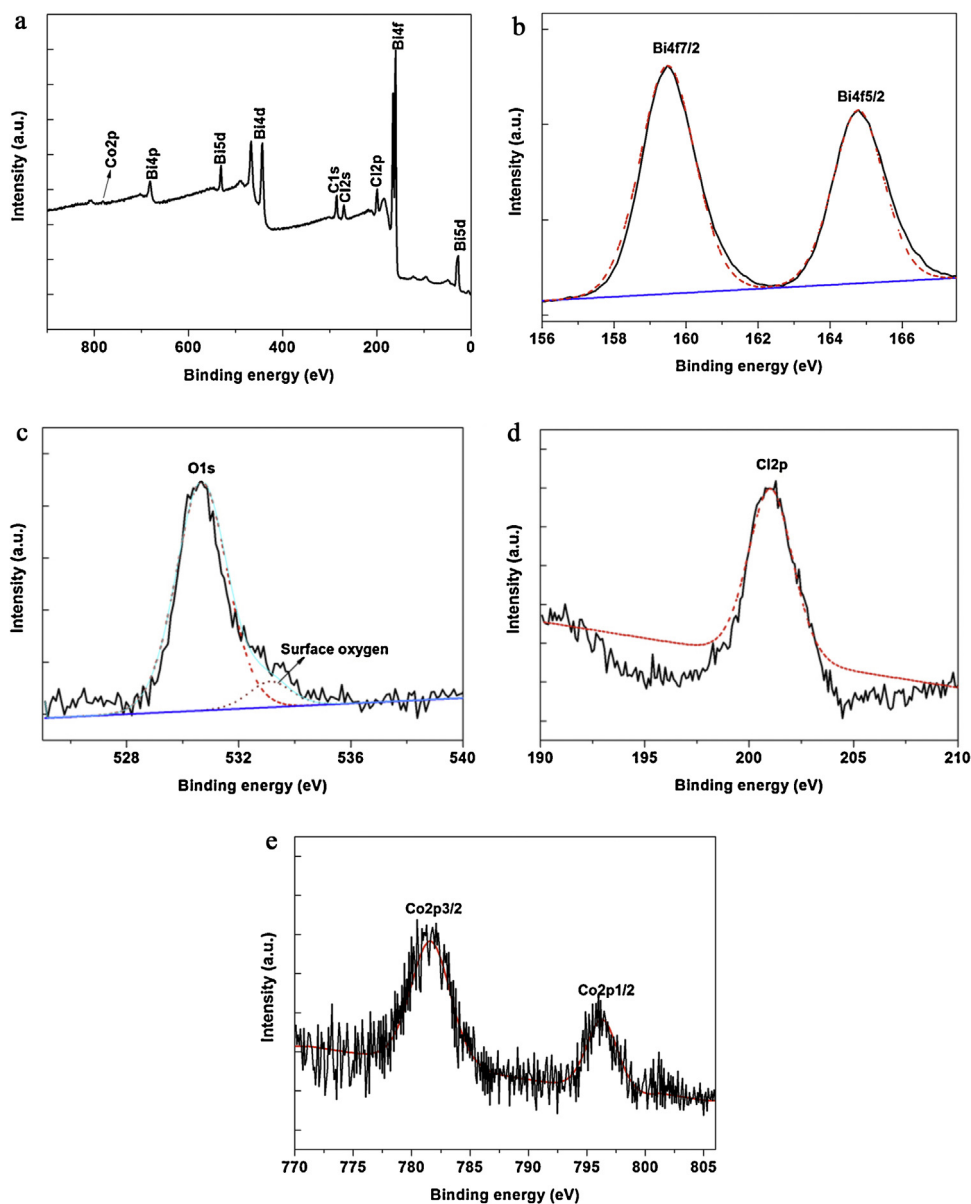


Fig. 2. XPS spectra of the 1.6 wt%  $\text{Co}_3\text{O}_4/\text{BiOCl}$  sample: survey scan (a), Bi 4f (b), O 1s (c), Cl 2p (d), and Co 2p (e).

the  $\text{Co}_3\text{O}_4$  nanoparticles and BiOCl nanoplates in the  $\text{Co}_3\text{O}_4/\text{BiOCl}$  heterostructured photocatalyst.

Generally speaking, the adsorption capacity of a photocatalyst is more or less related to its  $S_{\text{BET}}$ , and the higher adsorption capacity allows the photocatalyst to adsorb more reactant molecules in the pores for the photocatalytic reactions [36]. To differentiate the contribution of the  $S_{\text{BET}}$  of the samples to their photocatalytic activity, the  $S_{\text{BET}}$  of the samples were characterized by  $\text{N}_2$  adsorption–desorption method, and the results are shown in Fig. 4. The  $S_{\text{BET}}$  values of  $\text{Co}_3\text{O}_4/\text{BiOCl}$  samples containing 0, 0.4, 0.8, 1.2 and 1.6 wt%  $\text{Co}_3\text{O}_4$  are 32.94, 35.87, 34.66, 35.73 and 36.82  $\text{m}^2/\text{g}$ , respectively. As reported previously, the  $S_{\text{BET}}$  value of commercial P25- $\text{TiO}_2$  is about 50  $\text{m}^2/\text{g}$  [36]. Earlier reports [37,38] have demonstrated that the photogenerated electrons and holes as well as the adsorbed molecules might be able to diffuse more or less at the surface, causing more efficient photoreactions. Therefore, the higher  $S_{\text{BET}}$  value is expected to endow the prepared photocatalysts higher photocatalytic activity.

### 3.2. Photophysical properties of the $\text{Co}_3\text{O}_4/\text{BiOCl}$ heterostructured photocatalyst

The optical properties of the  $\text{Co}_3\text{O}_4/\text{BiOCl}$  samples with 0, 0.4, 0.8, 1.2, and 1.6 wt%  $\text{Co}_3\text{O}_4$  nanoparticles were studied by UV–vis diffuse reflectance spectroscopy and the results are plotted in Fig. 5. As shown in Fig. 5, visible light absorption ( $\lambda > 400 \text{ nm}$ ) of the  $\text{Co}_3\text{O}_4/\text{BiOCl}$  samples is much higher than that of pure BiOCl due to the contribution of  $\text{Co}_3\text{O}_4$  nanoparticles present on the surface of BiOCl nanoplates. As expected, pure BiOCl clearly shows an absorption edge at 360 nm, indicating that pure BiOCl can only be excited by UV light. By contrast, the  $\text{Co}_3\text{O}_4/\text{BiOCl}$  samples show an enhanced light absorbance in the wavelength range of 250–750 nm, evidencing that the  $\text{Co}_3\text{O}_4/\text{BiOCl}$  sample are active to UV as well as visible light.

The band gap energies ( $E_g$ ) of the  $\text{Co}_3\text{O}_4/\text{BiOCl}$  samples were calculated using the following equation [39,40]:

$$\alpha h\nu = A(h\nu - E_g)^{n/2} \quad (1)$$



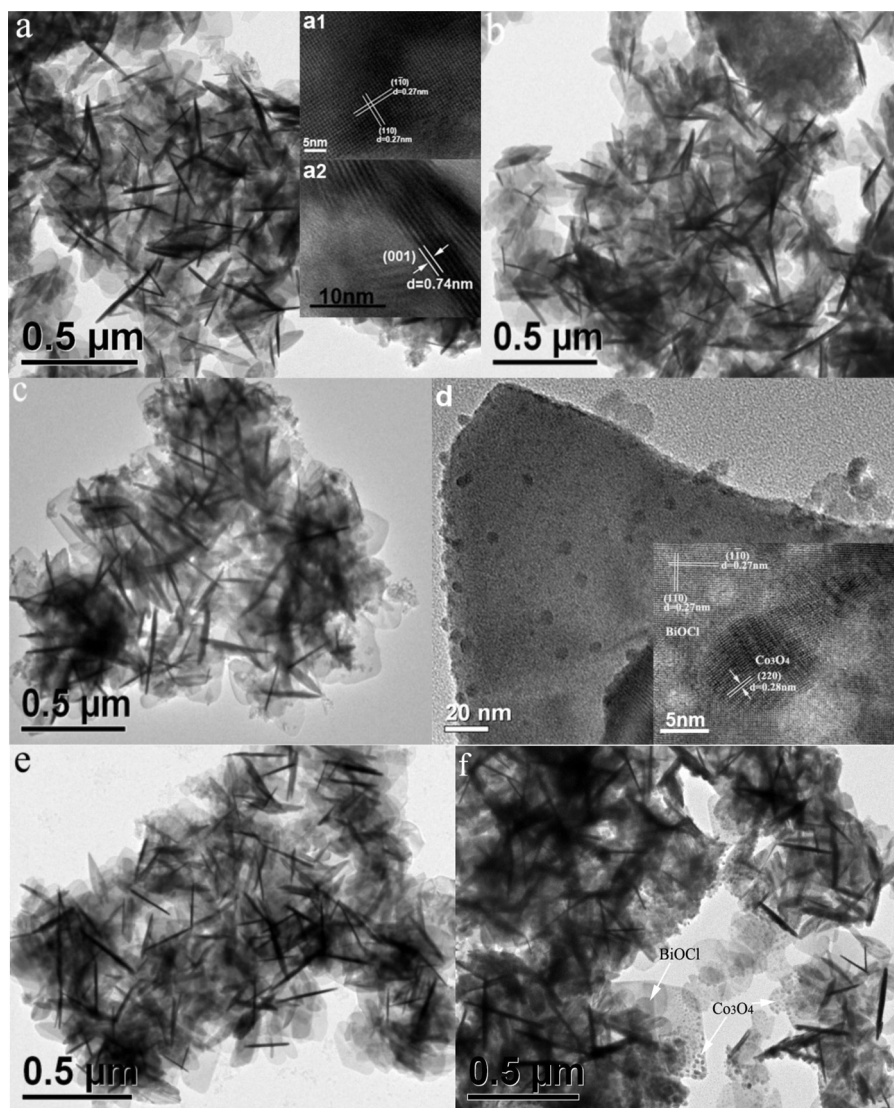


**Fig. 3.** TEM micrographs of the  $\text{Co}_3\text{O}_4/\text{BiOCl}$  samples with 0 wt% (a), 0.4 wt% (b), 0.8 wt% (c), 1.2 wt% (e), and 1.6 wt% (f)  $\text{Co}_3\text{O}_4$ . HRTEM image of the 0.8 wt%  $\text{Co}_3\text{O}_4/\text{BiOCl}$  sample (d, inset).

where  $\alpha$ ,  $h$ ,  $\nu$ ,  $E_g$ , and  $A$  are adsorption coefficient, Plank constant, light frequency, band gap, and a constant, respectively. As known,  $n$  is determined from the type of optical transition of a semiconductor, where  $n = 1$  for direct transition and  $n = 4$  for indirect transition. For  $\text{BiOCl}$  and  $\text{Co}_3\text{O}_4$ ,  $n = 1$  [41,14]. The calculated band gap energies of the samples are listed in Table 1.

### 3.3. Photocatalytic activity

The photocatalytic performance of  $\text{Co}_3\text{O}_4/\text{BiOCl}$  heterostructured photocatalysts prepared with 0, 0.4, 0.8, 1.2, and 1.6 wt%  $\text{Co}_3\text{O}_4$  nanoparticles was evaluated by the photodegradation of cationic (Rhodamine B) and ionic (methyl orange) organic dyes over the prepared samples under visible light irradiation ( $\lambda > 420 \text{ nm}$ ). To prove the electronegativity of the  $\{001\}$  facets, we first studied the adsorption behavior of the prepared samples using 20 mg/L RhB aqueous solution in the dark. Fig. 6 shows the adsorption behaviors of  $\text{Co}_3\text{O}_4/\text{BiOCl}$  heterostructured photocatalysts prepared with 0, 0.4, 0.8, 1.2, and 1.6 wt%  $\text{Co}_3\text{O}_4$  nanoparticles for RhB (20 mg/L RhB; 1 g/L photocatalyst sample) as a function of time in the dark. About 71% of RhB in aqueous solution was adsorbed by pure  $\text{BiOCl}$  nanoplates within 180 min. However, the adsorption of RhB was monotonously decreased with increasing the amount of  $\text{Co}_3\text{O}_4$

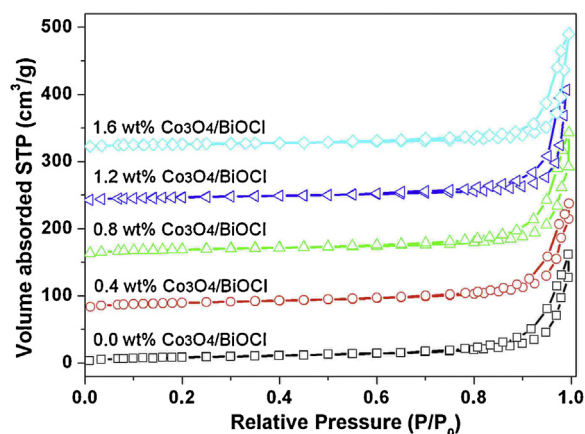


**Fig. 4.**  $\text{N}_2$  adsorption–desorption of the  $\text{Co}_3\text{O}_4/\text{BiOCl}$  samples with different amounts of  $\text{Co}_3\text{O}_4$  ranging from 0 to 1.6 wt%.

nanoparticles in the  $\text{Co}_3\text{O}_4/\text{BiOCl}$  samples. Only about 23.5% of RhB was adsorbed by the 1.6 wt%  $\text{Co}_3\text{O}_4/\text{BiOCl}$  sample. The  $\{001\}$  facets of  $\text{BiOCl}$  crystals are negative, and therefore, the total adsorbed amount of the positively-charged RhB molecules over the samples

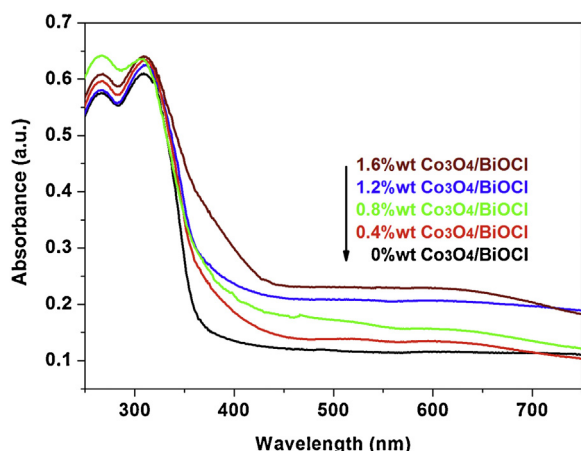


Fig. 5. UV-vis diffuse reflection spectra of the Co<sub>3</sub>O<sub>4</sub>/BiOCl samples with different amounts of Co<sub>3</sub>O<sub>4</sub> ranging from 0 to 1.6 wt%.

decreases with increasing the amount of Co<sub>3</sub>O<sub>4</sub> nanoparticles in the Co<sub>3</sub>O<sub>4</sub>/BiOCl sample. Although the photodegradation of RhB is resulted from the direct semiconductor photosensitization process, the adsorption process also has its own partial contribution.

Fig. 6b shows temporal changes in the UV-vis spectra of RhB aqueous solution after photodegradation reaction with the 0.8 wt% Co<sub>3</sub>O<sub>4</sub>/BiOCl sample under visible light. The concentration of RhB in aqueous solution decreases drastically within 12 min of

photodegradation reaction. The photodegradation profiles of RhB over the Co<sub>3</sub>O<sub>4</sub>/BiOCl heterostructured photocatalysts prepared with 0, 0.4, 0.8, 1.2, and 1.6 wt% Co<sub>3</sub>O<sub>4</sub> nanoparticles are shown in Fig. 6c. The blank test without a photocatalyst sample evidences that the RhB molecules are stable under visible light irradiation. A rapid decrease in the concentration of RhB is realized in the presence of the Co<sub>3</sub>O<sub>4</sub>/BiOCl samples. For pure *n*-type BiOCl sample, the total photodegradation of RhB can only reach 79% after 20 min of visible light irradiation. For the *p*-*n* heterojunctioned Co<sub>3</sub>O<sub>4</sub>/BiOCl samples, the total photodegradation of RhB rises significantly with increasing the amount of Co<sub>3</sub>O<sub>4</sub> nanoparticles up to 0.8 wt% and then slightly goes down with 1.2 and 1.6 wt%. Surprisingly, the complete photodegradation (100%) of RhB was achieved with the 0.8 wt% Co<sub>3</sub>O<sub>4</sub>/BiOCl sample within 12 min of visible light irradiation, whereas the samples prepared with 0.4, 1.2, and 1.6 wt% Co<sub>3</sub>O<sub>4</sub> nanoparticles show the total photodegradation of 98, 89, and 66% for RhB within 16 min irradiation, respectively.

The kinetics of RhB photodegradation was evaluated quantitatively by applying the pseudo-first-order model, as expressed by Eq. (1). This model is widely used for heterogeneous photocatalysis as the initial concentration of pollutant is low [4,7,24].

$$\frac{dC_t}{dt} = KC_t \text{ or } -\ln\left(\frac{C_t}{C_0}\right) = Kt \quad (2)$$

where  $C_t$  and  $C_0$  are the concentrations of RhB at time  $t$  and 0 (the time to obtain adsorption–desorption equilibrium) in aqueous solution,  $K$  is the pseudo-first-order rate constant, which can be obtained from the decrease of the peak intensity at 553 nm

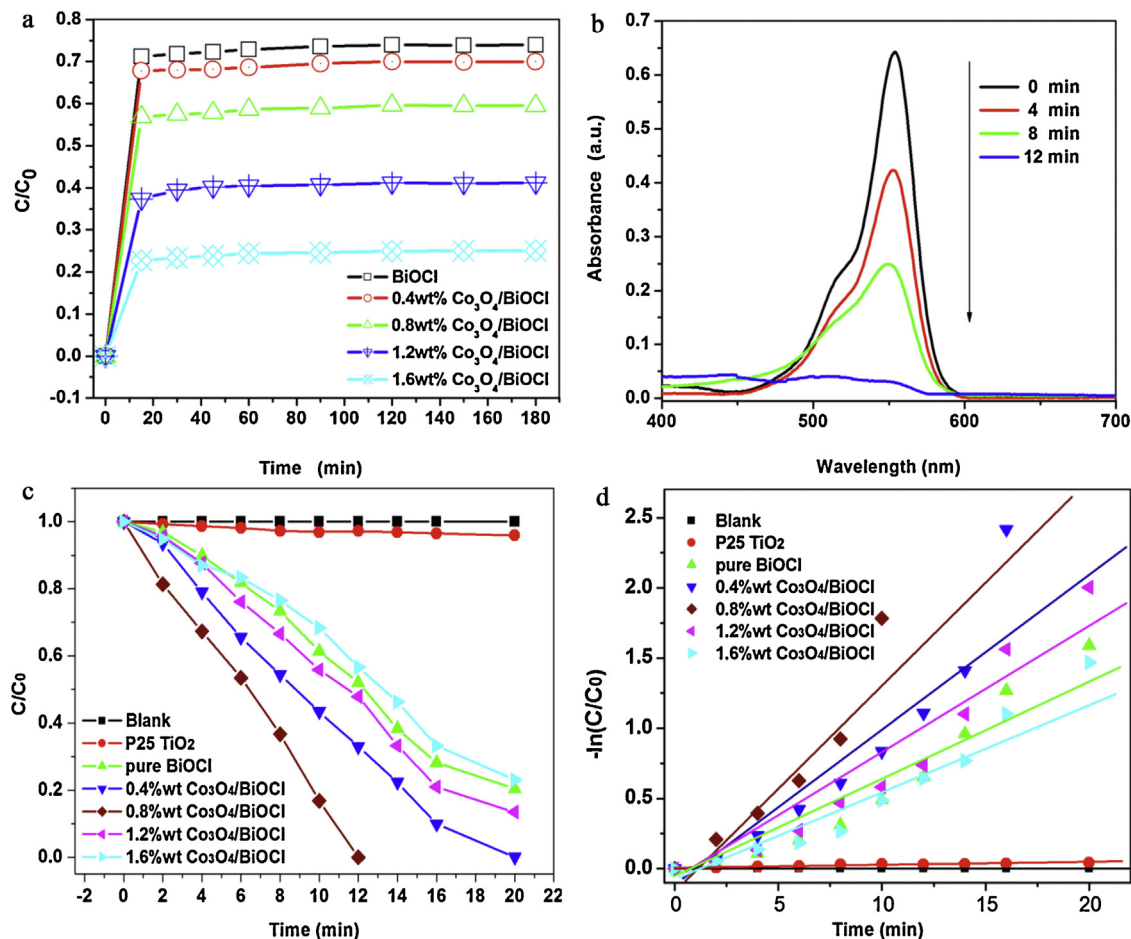


Fig. 6. Adsorption of RhB over the Co<sub>3</sub>O<sub>4</sub>/BiOCl samples in the dark (20 mg/L RhB, 1 g/L photocatalyst) (a), temporal changes in UV-vis spectra of RhB aqueous solution after photodegradation reaction with 0.8 wt% Co<sub>3</sub>O<sub>4</sub>/BiOCl sample under visible light (b), photodegradation profiles of RhB over the Co<sub>3</sub>O<sub>4</sub>/BiOCl samples under visible light (c), and kinetic linear simulation curves of RhB photodegradation over the samples (d).

**Table 1**  
Specific surface areas, band gap energies, and pseudo-first-order rate constants of the samples.

Samples	$S_{\text{BET}}$ ( $\text{m}^2/\text{g}$ )	Band gap (eV)	Photocatalytic activity (RhB)			Photocatalytic activity (MO)				
			$k_t^r$ ( $\text{min}^{-1}$ )	$k_t^r/S_{\text{BET}}$ ( $\text{g} \times \text{m}^{-2} \times \text{min}^{-1}$ )	$\alpha^r$	$\beta^r$	$k_t^m$ ( $\text{min}^{-1}$ )	$k_t^m/S_{\text{BET}}$ ( $\text{g} \times \text{m}^{-2} \times \text{min}^{-1}$ )	$\alpha^m$	$\beta^m$
P25-TiO <sub>2</sub>	50.00		0.002	$0.4 \times 10^{-4}$	1.0	115	0.002	$0.4 \times 10^{-4}$	1.0	125.0
Pure BiOCl	32.94	3.4	0.083	$2.5 \times 10^{-3}$	62.5	1.9	0.032	$9.7 \times 10^{-4}$	24.3	7.4
0.4 wt% Co <sub>3</sub> O <sub>4</sub> /BiOCl	35.87	3.3	0.132	$3.6 \times 10^{-3}$	90.0	1.3	0.170	$4.7 \times 10^{-3}$	117.5	1.5
0.8 wt% Co <sub>3</sub> O <sub>4</sub> /BiOCl	34.66	3.2	0.162	$4.6 \times 10^{-3}$	115.0	1.0	0.250	$7.2 \times 10^{-3}$	180.0	1.0
1.2 wt% Co <sub>3</sub> O <sub>4</sub> /BiOCl	35.73	3.2	0.102	$2.8 \times 10^{-3}$	70.0	1.7	0.129	$3.6 \times 10^{-3}$	90.0	2.0
1.6 wt% Co <sub>3</sub> O <sub>4</sub> /BiOCl	36.82	3.0	0.074	$2.0 \times 10^{-3}$	50.0	2.3	0.108	$2.9 \times 10^{-3}$	72.5	2.5

with time. To eliminate the influence of the  $S_{\text{BET}}$ s of the samples, we have adopted a parameter  $k_t^r/S_{\text{BET}}$  ( $\text{g} \times \text{m}^{-2} \times \text{min}^{-1}$ ) for the evaluation of photocatalytic performance of the prepared samples for RhB, and the pseudo-first-order rate constants were also calculated (Table 1). In fact, the heterojunction formed between Co<sub>3</sub>O<sub>4</sub> and BiOCl had a strong impact on the total photodegradation of RhB under visible light. The total photodegradation of RhB over the 0.8 wt% Co<sub>3</sub>O<sub>4</sub>/BiOCl sample is two times higher than that of pure BiOCl. As expected, commercial P25-TiO<sub>2</sub> sample shows insignificant photodegradation of RhB within 20 min of visible light irradiation.

However, the heterostructured photocatalyst has lower adsorption ability for MO, compared to RhB. Fig. 7 a shows the adsorption behavior of Co<sub>3</sub>O<sub>4</sub>/BiOCl heterostructured photocatalyst samples prepared with 0, 0.4, 0.8, 1.2, and 1.6 wt% Co<sub>3</sub>O<sub>4</sub> nanoparticles for MO (20 mg/L MO; 1 g/L photocatalyst) as a function of time in the dark. About 23% of MO in aqueous solution was adsorbed by pure BiOCl nanoplates within 180 min. Similarly, the total adsorption of MO over the Co<sub>3</sub>O<sub>4</sub>/BiOCl samples decreases with increasing the amount of Co<sub>3</sub>O<sub>4</sub> nanoparticles in the composite. Only about 14% of MO was adsorbed by 1.6 wt% Co<sub>3</sub>O<sub>4</sub>/BiOCl sample. The RhB and MO adsorption data obtained for the Co<sub>3</sub>O<sub>4</sub>/BiOCl samples conclude that the {001} facet was the dominantly exposure facet of BiOCl nanoplates and the heterojunction grew along the [001] crystallographic direction on the {001} facets. Although other heterojunctions were previously reported to have excellent photocatalytic activity for the photodegradation of MO [42], but the Co<sub>3</sub>O<sub>4</sub>/BiOCl shows it more obvious. Fig. 7b shows temporal changes in the UV-vis spectra of MO aqueous solution after photodegradation reaction with the 0.8 wt% Co<sub>3</sub>O<sub>4</sub>/BiOCl sample under visible light irradiation. As can be seen, the concentration of MO decreases sharply within 15 min of photodegradation reaction. The 0.8 wt% Co<sub>3</sub>O<sub>4</sub>/BiOCl sample degraded MO with the total photodegradation of 100% within 15 min of visible light irradiation, as shown in Fig. 7c, whereas the samples prepared with 0, 0.4, 1.2, and 1.6 wt% Co<sub>3</sub>O<sub>4</sub> nanoparticles showed the total photodegradation of 39, 99, 86, and 77% for MO, respectively. To eliminate the influence of the  $S_{\text{BET}}$ s of the samples, we have again used the parameter  $k_t^r/S_{\text{BET}}$  ( $\text{g} \times \text{m}^{-2} \times \text{min}^{-1}$ ) for the evaluation of photocatalytic performance of the prepared samples for MO, and the pseudo-first-order rate constants were also calculated (Table 1). The heterojunction formed between Co<sub>3</sub>O<sub>4</sub> and BiOCl had a strong influence on the photodegradation rate of MO under visible light. The total photodegradation of MO over the 0.8 wt% Co<sub>3</sub>O<sub>4</sub>/BiOCl sample is more than seven times higher than that of pure BiOCl. As expected, commercial P25-TiO<sub>2</sub> sample shows negligible photocatalytic activity for the photodegradation of MO under visible light.

In order to demonstrate excellent photocatalytic activity of the Co<sub>3</sub>O<sub>4</sub>/BiOCl heterostructured photocatalyst samples we have prepared, the photocatalytic performances of some heterojunctions reported previously are comparatively given in Table 2. According to Wang et al. [18] and Jiang et al. [20], the negative {001} facets terminated with oxygen can enhance the adsorption of cationic dye molecules, and the direct semiconductor photocatalysis is related to the surface structure rather than the specific surface area. Therefore, we believe that the results obtained from the photodegradation experiments with RhB are reasonable. But, for the photodegradation of MO, the Co<sub>3</sub>O<sub>4</sub>/BiOCl samples showed high photocatalytic activity under visible light because the photodegradation of MO might have taken place mainly via an indirect dye photosensitization process. Probably, the ionic MO molecules were not adsorbed on the negative {001} facets of BiOCl. Further analysis of the photodegradation of MO over the Co<sub>3</sub>O<sub>4</sub>/BiOCl samples under visible light suggests that the photodegradation process was similar to the direct semiconductor photocatalysis. That was not only



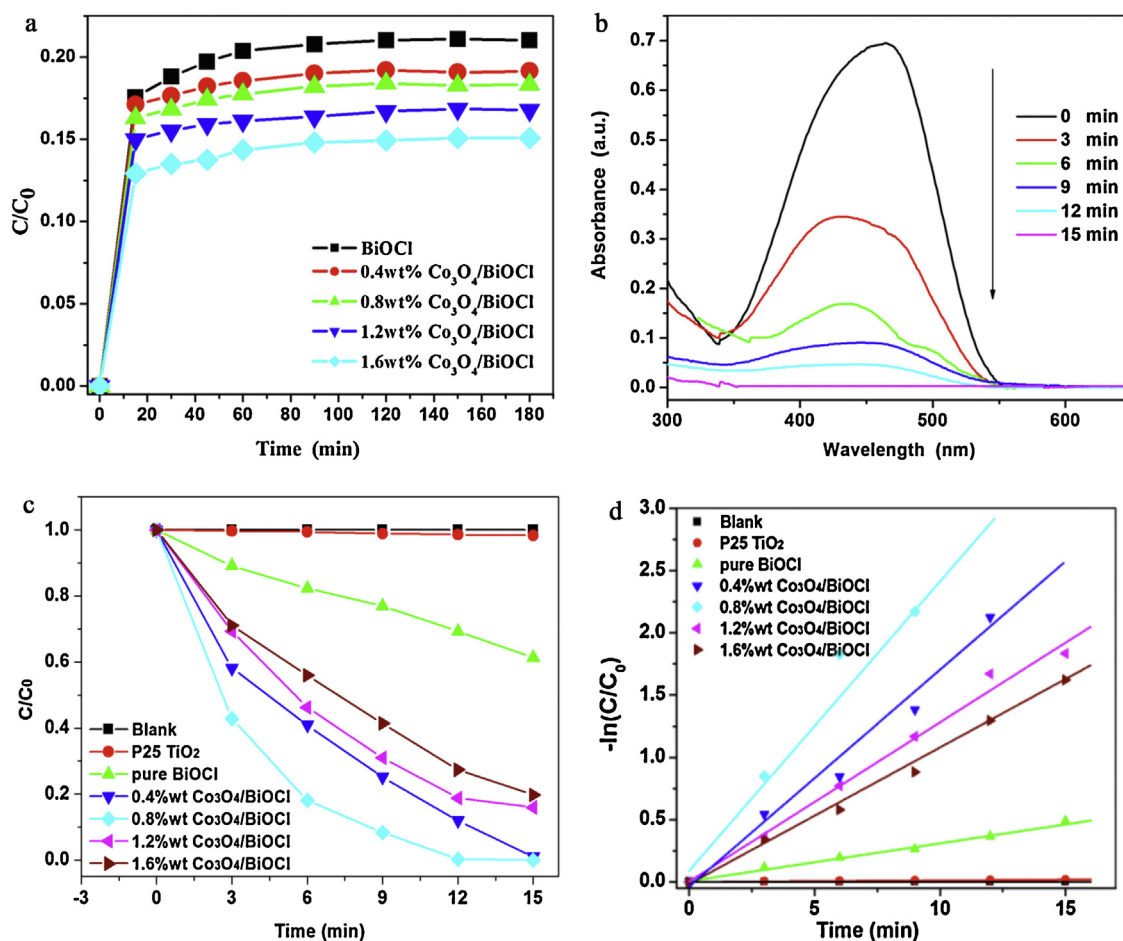


**Fig. 7.** Adsorption of MO over the  $\text{Co}_3\text{O}_4/\text{BiOCl}$  samples in the dark (20 mg/L MO, 1 g/L photocatalyst) (a), temporal changes in UV-vis spectra of MO aqueous solution after photodegradation reaction with 0.8 wt%  $\text{Co}_3\text{O}_4/\text{BiOCl}$  sample under visible light (b), photodegradation profiles of MO over the  $\text{Co}_3\text{O}_4/\text{BiOCl}$  samples under visible light (c), and kinetic linear simulation curves of MO photodegradation over the samples (d).

attributed to the heterojunction formed between the  $\text{Co}_3\text{O}_4$  and BiOCl phases, but also the {001} facets that might have embraced a promotional effect for the heterojunction by self-induced internal electric fields [20], enhancing the transformation of electrons and holes in the BiOCl and broadening the width of the heterojunction formed.

#### 3.4. Photostability of the $\text{Co}_3\text{O}_4/\text{BiOCl}$ heterostructured photocatalyst

To study the recombination of electron-hole pairs in the  $\text{Co}_3\text{O}_4/\text{BiOCl}$  heterostructured photocatalyst samples, pure BiOCl and 0.8 wt%  $\text{Co}_3\text{O}_4/\text{BiOCl}$  samples were subjected to photoluminescence (PL) measurements. The PL spectra of the samples are shown

in Fig. 8. As can be seen in Fig. 8a, the PL spectrum of pure BiOCl shows a strong emission; however, it is not active under UV light for the photodegradation reactions as the photo-generated electron-hole pairs recombine rapidly. By contrast, the PL spectrum of the 0.8 wt%  $\text{Co}_3\text{O}_4/\text{BiOCl}$  sample shows much lower intensity, indicating that the recombination of electron-hole pairs is restrained. On the basis of the obtained results, we can conclude that the  $\text{Co}_3\text{O}_4/\text{BiOCl}$  heterojunction could act as an active center for hindering the rapid recombination of photo-induced electron-hole pairs, enhancing the photocatalytic performance.

The photostability of  $\text{Co}_3\text{O}_4/\text{BiOCl}$  heterostructured photocatalyst was investigated by conducting five successive photodegradation experiments with 20 mg/L initial concentrations of RhB and MO aqueous solution and 1.0 g/L photocatalyst sample under

**Table 2**  
Photocatalytic performances of some composites.

Photocatalyst used and amount	Concentration and volume of dye solution	Visible light source	Photodegradation time (min)	Photodegradation (%)	Reference
$\text{Co}_3\text{O}_4/\text{BiOCl}$ (50 mg)	RhB, 10 mg/L, 50 mL	Halogen lamp, 400 W	12	100%	This work
$\text{BiOBr}/\text{BiHO}$ (100 mg)	RhB, 15 ppm, 200 mL	Xenon lamp, 300 W	60	47.3%	[11]
$\text{WO}_3/\text{BiOCl}$ (50 mg)	RhB, 30 mg/L, 50 mL	Halogen lamp, 1000 W	180	100%	[27]
$\text{Co}_3\text{O}_4/\text{Ag}_3\text{VO}_4$ (200 mg)	RhB, $10^{-5}$ mol/L, 100 mL	Xenon lamp, 500 W	80	99%	[31]
$\text{Co}_3\text{O}_4/\text{BiOCl}$ (50 mg)	MO, 10 mg/L, 50 mL	Halogen lamp, 400 W	15	100%	This work
$\text{Ag}/\text{WO}_3$ (100 mg)	MO, 10 mg/L, 50 mL	Xenon lamp, 500 W	180	93.3%	[35]
$\text{Ag}_3\text{PO}_4/\text{BiPO}_4$ (100 mg)	MO, 10 mg/L, 50 mL	Xenon lamp, 500 W	30	97%	[36]
$\text{g-C}_3\text{N}_4/\text{Bi}_2\text{WO}_6$ (150 mg)	MO, 10 mg/L, 50 mL	Xenon lamp, 500 W	180	99.9%	[43]



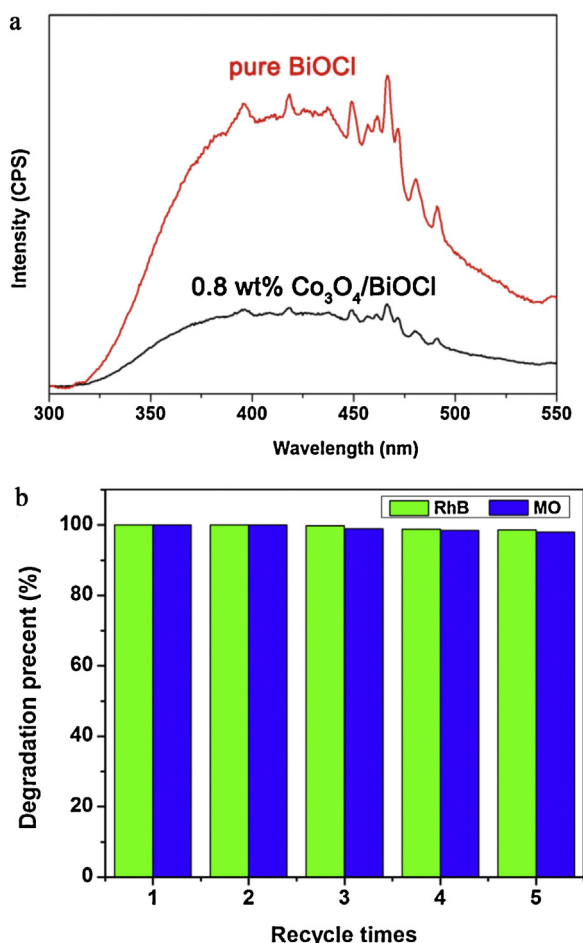


**Fig. 8.** PL emission spectra of pure BiOCl and 0.8 wt%  $\text{Co}_3\text{O}_4/\text{BiOCl}$  samples (a) and photocatalytic performance of 0.8 wt%  $\text{Co}_3\text{O}_4/\text{BiOCl}$  samples in five successive cycles of the photodegradation experiments of RhB (green) and MO (blue) (b).

visible light, and the results are plotted in Fig. 8b. For each experiment, the samples were collected, dried, and reused. As shown in Fig. 8b, the 0.8 wt%  $\text{Co}_3\text{O}_4/\text{BiOCl}$  sample retains high photocatalytic performance (>99%) in five successive photodegradation experiments with RhB (green) and MO (blue) due to its high photostability. The results from the photostability experiments confirm that the 0.8 wt%  $\text{Co}_3\text{O}_4/\text{BiOCl}$  heterostructured photocatalyst is very stable during five successive photodegradation reactions under visible light and can readily be recycled.

### 3.5. Mechanisms for the enhanced photocatalytic performance of the $\text{Co}_3\text{O}_4/\text{BiOCl}$ heterostructured photocatalyst

The enhancement of photocatalytic activity of the  $\text{Co}_3\text{O}_4/\text{BiOCl}$  heterostructured photocatalyst samples can be explained by assuming the formation of type-II  $p$ – $n$  heterojunction [4,28]. BiOCl is an  $n$ -type wide band gap ( $E_g = 3.4$  eV) semiconductor with the conduction band of 0.14 eV, and  $\text{Co}_3\text{O}_4$  is a  $p$ -type narrow band gap ( $E_g = 2.07$  eV) semiconductor with the conduction band of  $-0.37$  eV (Fig. 9 a). On the basis of the above-given values, it is possible to demonstrate here an energy band structure of  $\text{Co}_3\text{O}_4/\text{BiOCl}$  heterostructure schematically, as shown in Fig. 9. When  $\text{Co}_3\text{O}_4$  nanoparticles are deposited onto the surface of BiOCl nanoplates, a  $p$ – $n$  heterojunction is formed at the interface, and electrons transfer from the  $\text{Co}_3\text{O}_4$  to BiOCl until their Fermi levels are aligned (Fig. 9b), in other words, the thermal equilibrium state is reached in the semiconductor system. Hence, a band bending is expected

for the alignment of Fermi level (Fig. 9c). For the carrier concentration gradients, the holes from the  $p$ -type semiconductor diffuse into the  $n$ -type semiconductor while electrons so do contrary. As shown in Fig. 9d, theoretically, the inner electric field will be formed at the interface when the  $n$ -type and  $p$ -type semiconductors form a  $p$ – $n$  heterojunction. At the heterojunction in thermal equilibrium, the  $p$ -type and  $n$ -type regions have completely opposite charges, that is, the  $n$ -type region becomes positive while the  $p$ -type region becomes negative. Therefore, there is an opposing electric field ( $E_\xi$ ) created at the interface region. Furthermore, an equilibrium constant potential difference  $\Delta E_p$  across the transition region was also created. When the  $p$ – $n$  heterojunction is excited by visible light with the photon energy higher or equal to the band gap of  $p$ -type or/and  $n$ -type semiconductors, the photogenerated electrons can move to the CB of the  $n$ -type BiOCl and holes can move to the VB of the  $p$ -type  $\text{Co}_3\text{O}_4$  for the formation of the inner electric field in the  $\text{Co}_3\text{O}_4/\text{BiOCl}$  sample, restraining effectively the recombination of electron-hole pairs. As mentioned above, to study the effect of the amount of  $\text{Co}_3\text{O}_4$  nanoparticles on the photocatalytic activity of the  $\text{Co}_3\text{O}_4/\text{BiOCl}$  heterostructured photocatalyst is the main aim of the present work. Evidently, with increasing the amount of  $\text{Co}_3\text{O}_4$  nanoparticles, the number of heterojunctions increases significantly, and a greater amount of electron-hole pairs within the space charge region will be efficiently separated by the inner electric fields. However, in the samples with the amount of  $\text{Co}_3\text{O}_4$  beyond 0.8 wt%, the surplus carriers may recombine ultimately due to the reciprocal adherence of the  $\text{Co}_3\text{O}_4$  and BiOCl. As is known, BiOCl is not fully active to visible light to degrade the dye molecules. The results from the photodegradation experiments showed that pure BiOCl could also degrade the RhB and MO molecules under visible light. There is a significant role of photosensitization in photocatalysis process, in which the RhB and MO dye molecules can act as photosensitizers.

The aforementioned mechanisms of a heterojunction can explain the enhanced photocatalytic activity of the  $\text{Co}_3\text{O}_4/\text{BiOCl}$  heterostructured photocatalyst. However, the role of the {001} facets in interpreting the mechanisms of the enhancement of photocatalytic activity of the  $\text{Co}_3\text{O}_4/\text{BiOCl}$  sample should not be ignored. BiOCl has a unique layered structure, characterized by  $[\text{Bi}_2\text{O}_2]^{2+}$  slabs interleaved with double slabs of halogen atoms [20]. This architecture will induce the formation of internal static electric fields perpendicular to the  $[\text{Bi}_2\text{O}_2]^{2+}$  slabs and halogen anionic slabs in BiOCl [14], enhancing effectively the separation of the photo-induced electron-hole pairs along the [001] direction. As shown schematically in Fig. 9, the self-induced internal static electric fields are perpendicular to the BiOCl nanoplates with the {001} facets. Therefore, the charge separation or/and transformation in the heterojunction are promoted by the internal electric fields along the [001] direction of BiOCl. In addition, the width of the heterojunction might also be broadened by the formation of the self-induced internal electric fields of BiOCl.

On the basis of the experimental results demonstrated above, a possible mechanism for the enhanced photodegradation of RhB and MO over the  $\text{Co}_3\text{O}_4/\text{BiOCl}$  heterostructured photocatalyst under visible light is illustrated in Fig. 10. Generally, the semiconductor-based photocatalysis process involves the photo-excitation of a semiconductor, the separation of photo-induced electron-hole pairs, bulk diffusion, surface transfer of photo-induced charge carriers, the generation of active species, and pollutant degradation [1]. With a photon having energy equal to or higher than the band gap energy of  $\text{Co}_3\text{O}_4$ ,  $\text{Co}_3\text{O}_4$  is excited by visible light to generate electron-hole pairs. As demonstrated in Figs. 9 and 10, the photo-induced electrons transfer easily from the CB of  $\text{Co}_3\text{O}_4$  to the CB of BiOCl due to the electrostatic field ( $E_\xi$ ) of the band bending region in the heterojunction. The photo-induced electrons then react with  $\text{O}_2$  and  $\text{H}_2\text{O}$  adsorbed onto the surface of heterostructured

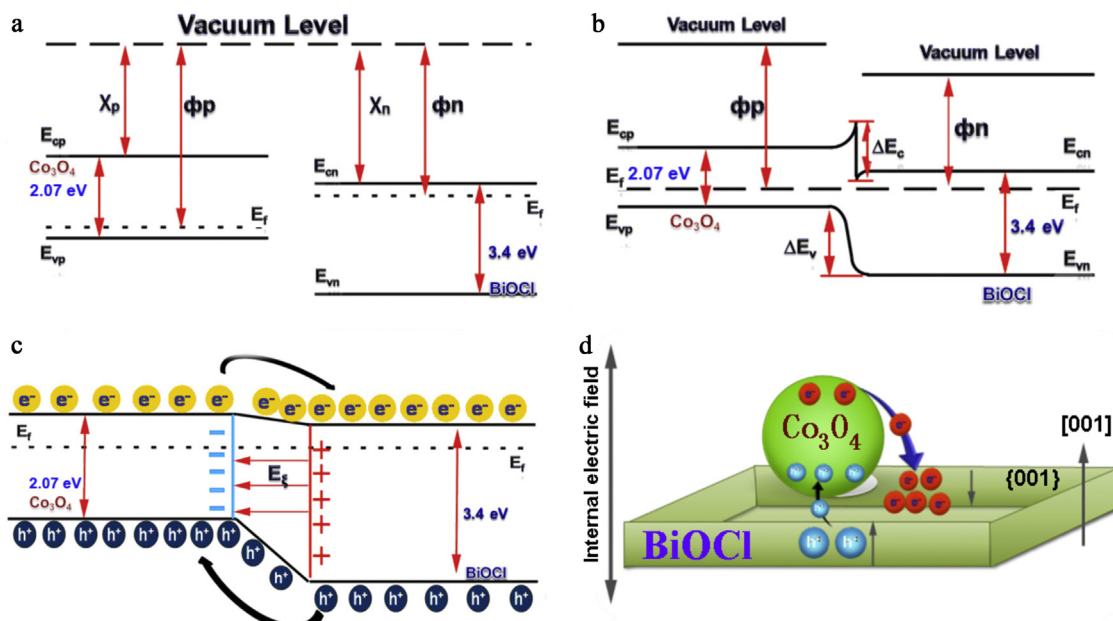


**Fig. 9.** Schematic illustration of possible photodegradation mechanisms involving the indirect (a) and direct (b) semiconductor photosensitization processes. Possible photodegradation mechanism of RhB and MO over the  $\text{Co}_3\text{O}_4/\text{BiOCl}$  photocatalyst (c) and a model showing the synergism of the internal electric fields and the heterojunction (d).

photocatalyst samples, and as a result, superoxide radical anions ( $\bullet\text{O}_2^-$ ,  $\bullet\text{OH}$ , etc.) are produced. The photo-induced holes are trapped by  $\text{H}_2\text{O}$  and  $\text{OH}^-$  to further produce  $\bullet\text{OH}$  and  $\text{OH}^-$  species.

For the photodegradation of RhB over the  $\text{Co}_3\text{O}_4/\text{BiOCl}$  heterostructured photocatalyst samples, the mechanism is considered to be a direct semiconductor photosensitization process, as shown in Fig. 10a. By contrast, the photodegradation of MO over the  $\text{Co}_3\text{O}_4/\text{BiOCl}$  heterostructured photocatalyst samples is recognized as an indirect semiconductor photosensitization process, as shown in Fig. 10b. That is to say, the dye molecules also absorb the

photon energy to generate the electrons which ultimately transfer to the CB of *n*-type  $\text{BiOCl}$  for the direct semiconductor photosensitization process. It should be mentioned here that there is an essential role belonging to the dye in the photocatalysis process where the dye molecules act as photosensitizers. Under visible light, singlet and triplet states (donated as  $\text{dye}^*$ ) are produced. During the photocatalysis process, the photo-induced electron-hole pairs are separated efficiently at the type-II *p-n*  $\text{Co}_3\text{O}_4/\text{BiOCl}$  heterojunction's interface and further participate in the RhB photodegradation reactions. The  $\text{dye}^*$  is converted to the radical cation

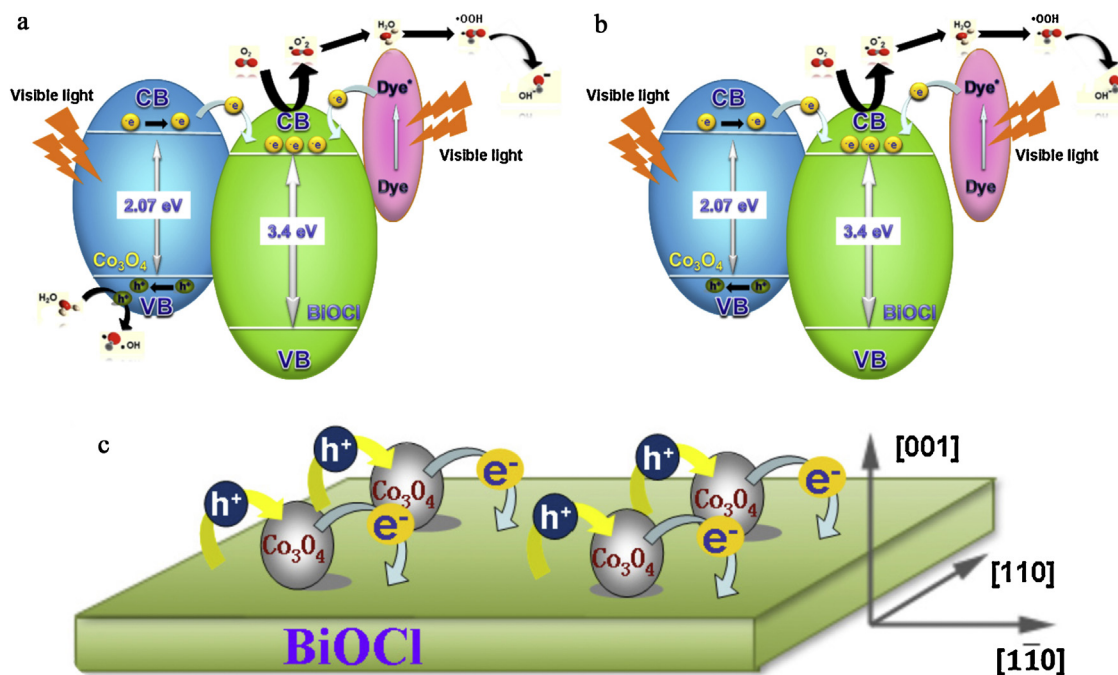
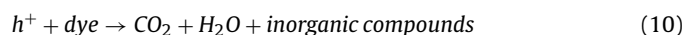
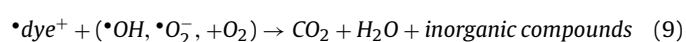
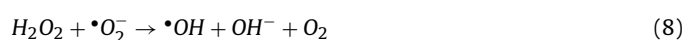
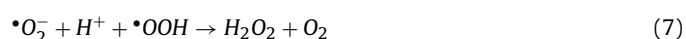
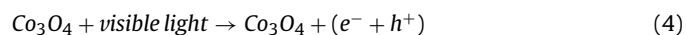
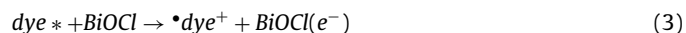


**Fig. 10.** The energy band structure of  $\text{BiOCl}$  and  $\text{Co}_3\text{O}_4$  before the formation of a heterojunction (a), the energy band structure of  $\text{Co}_3\text{O}_4/\text{BiOCl}$  heterojunction at equilibrium (b), and the abbreviated mechanism of the formed heterojunction and the transformation of electron-hole pairs (c).

•dye<sup>+</sup>, and BiOCl is converted to BiOCl(e<sup>-</sup>). Then, the radical cation •dye<sup>+</sup> ultimately reacts with oxygen radicals to yield the degraded products, such as CO<sub>2</sub>, H<sub>2</sub>O, and inorganic compounds [44]. Therefore, the Co<sub>3</sub>O<sub>4</sub>/BiOCl heterostructured photocatalyst shows higher photocatalytic activity compared to individual ones under visible light. The mechanism (direct semiconductor photosensitization) for the photodegradation of RhB and MO over the Co<sub>3</sub>O<sub>4</sub>/BiOCl heterostructured photocatalyst can be described in Eqs. (2)–(10), as follows:



The mechanism involving the indirect semiconductor photosensitization has the same photodegradation reaction pathway, including the photo-excitation of dye molecules, transfer of photo-induced electrons into the CB of *n*-type BiOCl, the reaction of the photo-induced electrons with O<sub>2</sub> and H<sub>2</sub>O adsorbed on the surface of heterostructured photocatalyst, the photodegradation of pollutants. The main difference between these two mechanisms is that the VB of *p*-type Co<sub>3</sub>O<sub>4</sub> semiconductor is not involved in the photodegradation reaction in the indirect semiconductor photosensitization process. Therefore, the photodegradation mechanism of MO over the Co<sub>3</sub>O<sub>4</sub>/BiOCl heterostructured photocatalyst under visible light lacks for the generation of •O<sub>2</sub><sup>-</sup> combined with h<sup>+</sup> on the valance band.

A more important prerequisite is the direct constant between the dye molecules and the semiconductor for the injection of photo-induced electrons into the semiconductor band [45]. Thus, the photocatalytic activity depends on the interface properties between the dye molecules and Co<sub>3</sub>O<sub>4</sub>/BiOCl heterostructured photocatalyst. As mentioned above, the photodegradation of RhB over the Co<sub>3</sub>O<sub>4</sub>/BiOCl heterostructured photocatalyst is much higher than that of MO due to the identical electronegativity of MO molecules and the {001} facets of BiOCl. Further, the enhancement of photocatalytic activity of Co<sub>3</sub>O<sub>4</sub>/BiOCl heterostructured photocatalyst for the photodegradation of MO will be discussed. It is indispensable to emphasize that the self-induced internal electric fields can induce more efficient separation of electron-hole pairs transferring along the [001] direction in the BiOCl nanoplates, as shown in Fig. 10c. That is, the internal electric fields will enhance the efficiency of Co<sub>3</sub>O<sub>4</sub>/BiOCl heterojunction. The photo-generated electrons and holes are fleetly mobilized in the BiOCl semiconductor, e.g., electrons transfer rapidly onto the surface, quickening the rate of O<sub>2</sub><sup>-</sup> species. Meanwhile, the self-induced internal electric fields may also broaden the area of the electric field (*E<sub>z</sub>*) along the [001] direction of BiOCl, inhibiting the recombination of photo-induced electron-hole pairs to increase the photodegradation of MO. Therefore, a synergetic effect of the internal electric field along the [001] direction and the heterojunction of the [001] facets may account for the efficient photodegradation of RhB and MO over the Co<sub>3</sub>O<sub>4</sub>/BiOCl heterostructured photocatalyst under visible light.

## 4. Conclusions

In summary, the Co<sub>3</sub>O<sub>4</sub>/BiOCl heterostructured photocatalyst was synthesized by a simple chemical co-precipitation method. The effect of the amount of Co<sub>3</sub>O<sub>4</sub> nanoparticles on the enhancement of photocatalytic performance of Co<sub>3</sub>O<sub>4</sub>/BiOCl heterostructured photocatalyst was studied. Among all the samples prepared, the 0.8 wt% Co<sub>3</sub>O<sub>4</sub>/BiOCl sample demonstrated the highest photocatalytic activity for the photodegradation of RhB and MO under visible light. The enhanced photocatalytic performance of Co<sub>3</sub>O<sub>4</sub>/BiOCl sample is attributed to the formation of the Co<sub>3</sub>O<sub>4</sub>/BiOCl heterojunction at the interface and the self-induced internal electric fields along the [001] direction of BiOCl. The formed Co<sub>3</sub>O<sub>4</sub>/BiOCl heterojunction could efficiently hinder the recombination of electron-hole pairs and facilitate the transfer of the photo-generated electrons and holes. The BiOCl nanoplates with the exposed {001} facets also contributed to the enhancement of photocatalytic activity of Co<sub>3</sub>O<sub>4</sub>/BiOCl sample, particularly for the photodegradation of RhB. Our investigations on the enhancement of photocatalytic performance of other heterojunctioned photocatalysts with different exposed crystal facets are in process.

## Acknowledgments

This work was supported by the National Natural Science Foundation of China (Program nos. 51102160 and 51272148) and the State Ministry of Education College Students' Innovative Projects (Program No. 201310718034, cx13035). MH would like to thank the Japan Society for the Promotion of Science (JSPS) for financial support.

## References

- [1] H. Tong, S. Ouyang, Y. Bi, N. Umezawa, M. Oshikiri, J.H. Ye, *Adv. Mater.* 24 (2012) 229–251.
- [2] A. Fujishima, K. Honda, *Nature* 238 (1972) 37–38.
- [3] D.H. Yoo, T.V. Cuong, V.H. Luan, N.T. Khoa, E.J. Kim, S.H. Hur, S.H. Hahn, *J. Phys. Chem. C* 116 (2012) 7180–7184.
- [4] D. Sarkar, C.K. Ghosh, S. Mukherjee, K.K. Chattopadhyay, *ACS Appl. Mater. Interfaces* 5 (2013) 331–337.
- [5] H. Huang, D. Li, Q. Lin, W. Zhang, Y. Shao, Y. Chen, M. Sun, X. Fu, *Environ. Sci. Technol.* 43 (2009) 4164–4168.
- [6] S. Liu, J. Wu, X. Liu, R. Jiang, *J. Mol. Catal. A* 332 (2010) 84–92.
- [7] Z. Zhang, C. Shao, X. Li, C. Wang, M. Zhang, Y. Liu, *ACS Appl. Mater. Interfaces* 2 (2010) 2915–2923.
- [8] H.G. Kim, D.W. Hwang, J.S. Lee, *J. Am. Chem. Soc.* 126 (2004) 8912–8913.
- [9] M. Vivar, M. Fuentes, N. Dodd, J. Scott, I. Skryabin, K. Srihar, *Solar Energy Mater. Solar Cells* 98 (2012) 260–266.
- [10] L. Chen, S.F. Yin, S.L. Luo, R. Huang, Q. Zhang, T. Hong, P.C.T. Au, *Ind. Eng. Chem. Res.* 51 (2012) 6760–6768.
- [11] S. Shenawi-Khalil, V. Uvarov, S. Fronton, I. Popov, Y. Sasson, *J. Phys. Chem. C* 116 (2012) 11004–11012.
- [12] S.Y. Chai, Y.J. Kim, M.H. Jung, A.K. Chakraborty, D. Jung, W.I. Lee, *J. Catal.* 262 (2009) 144–149.
- [13] H. Huang, D. Li, Q. Lin, Y. Shao, W. Chen, Y. Hu, Y. Chen, X. Fu, *J. Phys. Chem. C* 113 (2009) 14264–14269.
- [14] K.L. Zhang, C.M. Liu, F.Q. Huang, C. Zheng, W.D. Wang, *Appl. Catal. B* 68 (2006) 125–129.
- [15] W. Wang, F. Huang, X. Lin, J. Yang, *Catal. Commun.* 9 (2008) 8–12.
- [16] H. An, Y. Du, T. Wang, C. Wang, W. Hao, J. Zhang, *Rare Met.* 27 (2008) 243–250.
- [17] R.J. Talling, R.J. Dashwood, M. Jackson, S. Kuramoto, D. Dye, *Scr. Mater.* 59 (2008) 669–672.
- [18] D.H. Wang, G.Q. Gao, Y.W. Zhang, L.S. Zhou, A.W. Xu, W. Chen, *Nanoscale* 4 (2012) 7780–7785.
- [19] L. Ye, L. Zan, L. Tian, T. Peng, J. Zhang, *Chem. Commun.* 47 (2011) 6951–6953.
- [20] J. Jiang, K. Zhao, X. Xiao, L. Zhang, *J. Am. Chem. Soc.* 134 (2012) 4473–4476.
- [21] Y. Chen, R. Huang, D. Chen, Y. Wang, W. Liu, X. Li, Z. Li, *ACS Appl. Mater. Interfaces* 4 (2012) 2273–2279.
- [22] A.K. Chakraborty, S.B. Rawal, S.Y. Han, S.Y. Chai, W.I. Lee, *Appl. Catal. A* 407 (2011) 217–223.
- [23] F. Dong, Y. Sun, M. Fu, Z. Wu, S.C. Lee, *J. Hazard. Mater.* 219–220 (2012) 26–34.
- [24] S. Shamaila, A.K.L. Sajjad, F. Chen, J. Zhang, *J. Colloid Interface Sci.* 356 (2011) 465–472.
- [25] X. Chang, G. Yu, J. Huang, Z. Li, S. Zhu, P. Yu, C. Cheng, S. Deng, G. Ji, *Catal. Today* 153 (2010) 193–199.



- [26] M. Long, W. Cai, J. Cai, B. Zhou, X. Chai, Y. Wu, *J. Phys. Chem. B* 110 (2006) 20211–20216.
- [27] H.A.E. Hagelin-Weaver, G.B. Hoflund, D.M. Minahan, G.N. Salaita, *Appl. Surf. Sci.* 235 (2004) 420–448.
- [28] E. Barrera, I. González, T. Viveros, *Solar Energy Mater. Solar Cells* 51 (1998) 69–82.
- [29] L. Zhang, Y. He, P. Ye, W. Qin, Y. Wu, T. Wu, *Mater. Sci. Eng. B* 178 (2013) 45–52.
- [30] C. Yu, K. Yang, J.C. Yu, F. Cao, X. Li, X. Zhou, *J. Alloys Compd.* 509 (2011) 4547–4552.
- [31] G.S. Armatas, A.P. Katsoulidis, D.E. Petrakis, P.J. Pomonis, M.G. Kanatzidis, *Chem. Mater.* 22 (2010) 5739–5746.
- [32] C. Ma, D. Wang, W. Xue, B. Dou, H. Wang, Z. Hao, *Environ. Sci. Technol.* 45 (2011) 3628–3634.
- [33] W.Q. Fang, J.Z. Zhou, J. Liu, Z.G. Chen, C. Yang, C.H. Sun, G.R. Qian, J. Zou, S.Z. Qiao, H.G. Yang, *Chem. Eur. J.* 17 (2011) 1423–1427.
- [34] X.H. Yang, Z. Li, G. Liu, J. Xing, C. Sun, H.G. Yang, C. Li, *CrystEngComm* 13 (2011) 1378–1383.
- [35] M. Yin, Y. Gu, I.L. Kuskovsky, T. Andelman, Y. Zhu, G.F. Neumark, S. O'Brien, *J. Am. Chem. Soc.* 126 (2004) 6206–6207.
- [36] J.F. Guo, B.W. Ma, A.Y. Yin, K.N. Fan, W.L. Dai, *Appl. Catal. B* 101 (2011) 580–586.
- [37] H. Wang, Y. Wu, B.Q. Xu, *Appl. Catal. B* 59 (2005) 139–146.
- [38] J.H. Xu, J. Li, W.L. Dai, Y. Cao, H. Li, K. Fan, *Appl. Catal. B* 79 (2008) 72–80.
- [39] W.R. Zhao, Y. Wang, Y. Yang, J. Tang, Y.A. Yang, *Appl. Catal. B* 115–116 (2012) 90–99.
- [40] H. Lin, C.P. Huang, W. Li, C. Ni, S.I. Shah, Y.H. Tseng, *Appl. Catal. B* 68 (2006) 1–11.
- [41] H.X. Jin, X.J. Gu, B. Hong, L.H. Lin, C.Y. Wang, D.F. Jin, X.L. Peng, X.Q. Wang, H.L. Ge, *J. Phys. Chem. C* 116 (2012) 13374–13381.
- [42] R. Alanís-Oaxaca, J. Jiménez-Becerril, *J. Mex. Chem. Soc.* 54 (2010) 164–168.
- [43] L. Ge, C. Han, J. Liu, *Appl. Catal. B* 108–109 (2011) 100–107.
- [44] W.J. Kim, D. Pradhan, B.K. Min, Y. Sohn, *Appl. Catal. B* 147 (2014) 711–725.
- [45] S. Ge, L. Zhang, *Environ. Sci. Technol.* 45 (2011) 3027–3033.